

Bioinspired Spiky Peroxidase-Mimics for Localized Bacterial Capture and Synergistic Catalytic Sterilization

Ye Yang, Xizheng Wu, Lang Ma, Chao He, Sujiao Cao, Yanping Long, Jianbo Huang, Raul D. Rodriguez, Chong Cheng,* Changsheng Zhao,* and Li Qiu*

Besides the pandemic caused by the coronavirus outbreak, many other pathogenic microbes also pose a devastating threat to human health, for instance, pathogenic bacteria. Due to the lack of broad-spectrum antibiotics, it is urgent to develop nonantibiotic strategies to fight bacteria. Herein, inspired by the localized "capture and killing" action of bacteriophages, a virus-like peroxidase-mimic (V-POD-M) is synthesized for efficient bacterial capture (mesoporous spiky structures) and synergistic catalytic sterilization (metalorganic-framework-derived catalytic core). Experimental and theoretical calculations show that the active compound, MoO3, can serve as a peroxocomplex-intermediate to reduce the free energy for catalyzing H₂O₂, which mainly benefits the generation of •OH radicals. The unique virus-like spikes endow the V-POD-M with fast bacterial capture and killing abilities (nearly 100% at 16 µg mL⁻¹). Furthermore, the in vivo experiments show that V-POD-M possesses similar disinfection treatment and wound skin recovery efficiencies to vancomycin. It is suggested that this inexpensive, durable, and highly reactive oxygen species (ROS) catalytic active V-POD-M provides a promising broad-spectrum therapy for nonantibiotic disinfection.

The global pandemic caused by the outbreak of coronavirus has aroused tremendous attention across broad scientific communities. Besides the coronavirus pandemic, many other pathogenic microbes also pose a devastating threat to human health. For instance, pathogenic bacteria have infected millions of people and caused almost one million deaths every year worldwide. [1–3] Currently, due to the lack of broad-spectrum antibiotics and the development of drug resistance, it is urgent to develop more effective strategies to fight against bacterial

infections.^[4–10] Nature has created an efficient sterilization model, i.e., the in situ bacterial capture and killing process via bacteriophages. The bacteriophage is a virus with a unique spiny tail foot; in general, it can capture bacteria and subsequently release nucleic acid to achieve replication and kill bacteria. We define this two-steps process as the localized "capture and killing" (LCK) action. Therefore, it is believed that this bioinspired LCK action may provide massive possibilities for developing efficient disinfection strategies as alternatives to conventional clinical antibiotic treatments.

Two concepts must be carefully designed and integrated to construct the bionic nanosystem with LCK action. i) Developing the spiky nanostructures to enhance the interactions between nanomaterials and pathogenic bacteria; [11,12] meanwhile, the spiky structure must be mesoporous to load and release bacte-

ricidal substances.^[13] ii) Second, developing an efficient and robust bactericidal system without using any antibiotics.^[14–18] Compared to many traditional bactericidal molecules, antibacterial strategies based on reactive oxygen species (ROS) have been intensively studied.^[19] Due to its short life cycle, ROS can only cause irreversible damage to substances immediately around it. This spatially confined activity helps to develop targeted applications as well as guarantee excellent biocompatibility during usage.^[20,21] Moreover, the molecular weight of ROS is very

Y. Yang, X. Z. Wu, Prof. L. Ma, Dr. C. He, Dr. S. J. Cao, Y. P. Long, J. B. Huang, Prof. C. Cheng, Prof. C. S. Zhao, Prof. L. Qiu College of Polymer Science and Engineering State Key Laboratory of Polymer Materials Engineering Department of Ultrasound West China Hospital Sichuan University Chengdu 610065, China E-mail: chong.cheng@scu.edu.cn; zhaochsh70@scu.edu.cn; qiulihx@scu.edu.cn
Prof. R. D. Rodriguez Tomsk Polytechnic University Lenina ave. 30, Tomsk 634034, Russia

Takustrasse 3, 14195 Berlin, Germany
Prof. C. S. Zhao
College of Biomedical Engineering
National Engineering Research Center for Biomaterials
Sichuan University
Chengdu 610064, China
Prof. C. S. Zhao
College of Chemical Engineering
Sichuan University
Chengdu 610065, China

Department of Chemistry and Biochemistry

The ORCID identification number(s) for the author(s) of this article can be found under https://doi.org/10.1002/adma.202005477.

DOI: 10.1002/adma.202005477

Prof. C. Cheng

Freie Universität Berlin





www.advmat.de

small, which can quickly diffuse through the mesoporous spiky structures and damage the targeted pathogens.^[22] Therefore, the ROS-based spiky nanosystem is very suitable for mimicking the LCK action to combat pathogenic bacteria.

Inspired by the peroxidase (POD) in the immune system, many synthetic POD-mimics (POD-M) show promising activities for ROS generation, [23-27] especially metal-organic framework (MOF)-derived POD-M.^[28-31] MOFs possess uniformly distributed molecular/atom-level catalytic centers and porous nanostructures, which can promote the transport and catalysis of POD substrates; thus, now, they are emerging as one of the most promising ROS-catalytic nanoplatforms.[32-37] However, when applied at a very low dosage, such POD-M catalysts show insufficient activity to kill bacteria, as the adsorbate binding energy between the metal ions and H2O2 substances significantly affects the ROS catalytic activity.[19] Thereby, loading other active cocatalysts to reduce the energy barrier required for ROS generation and achieving the cascaded POD-mimetic catalytic process can provide essential pathways to achieve high ROS catalytic activity at low dosage.

To overcome the bionic challenge on the integration of high ROS catalytic activity and spiky nanostructures, inspired by the LCK action of bacteriophage, in this study, for the first time, we report the synthesis of a virus-like peroxidase-mimics (V-POD-M) for efficient bacterial capture (via mesoporous-silica-based spiky structures) and synergistic catalytic sterilization (via MOF-derived cascaded ROS catalytic core). Experimental and theoretical calculations show that the loaded MoO3 in MOFs can serve as peroxo-complex-intermediate to accelerate the ROS catalytic activities, which facilitate the ·OH radical generation reaction. The integrated unique virus-like mesoporous spikes and high ROS catalytic activity endow the V-POD-M with rapid bacterial capture and high killing ratio. Thereby, in the presence of small amounts of H_2O_2 (0.1 × 10⁻³ M), the V-POD-M possesses efficient disinfection performance (nearly 100%) for both in vivo and in vitro experiments at very low concentrations (16 µg mL⁻¹), which is similar to the treatment and wound recovery efficiencies of vancomycin. We suggest that this inexpensive, durable, and highly ROS catalytic active V-POD-M provides a promising broad-spectrum therapy for nonantibiotic disinfection.

First, the MOF-derived cascaded ROS catalytic core is synthesized, a Cu (II)-based MOF is chosen to yield the POD-mimic catalysis. [38–40] For the cascaded POD-mimetic catalytic reaction, the Mo/W-based transition metal compound has been reported to show a high affinity to H_2O_2 and reduce the energy barrier. [41–43] Therefore, we further loaded phosphomolybdic acid hydrate into the Cu (II)-based MOF to yield the POD-M with the formula $[Cu_2(BTC)_{4/3}(H_2O)_2]_6[H_3PMo_{12}O_{40}]$, [44] which consists of the catalytic centers of Cu (II) and MoO₃ (Figure 1a and Figure S1, Supporting Information). Then, to improve the bacterial capture ability, a virus-like spiky and mesoporous silica shell with many epitaxial nanostructures (Figure 1b and Figure S2, Supporting Information) is coated onto the surface of POD-M by a single-channel oriented assembly method, and the final product is denoted as V-POD-M.

Typical high-resolution scanning electron microscopy (HR-SEM) and transmission electron microscopy (HR-TEM) imaging results demonstrate an octahedron morphology of

POD-M and the virus-like shell structures of V-POD-M, preliminarily supporting the concept we proposed (Figure 1c,c-1,d,d-1 and Figures S2 and S3, Supporting Information). The as-prepared POD-M (\approx 2.6 μ m) and V-POD-M (\approx 2.9 μ m) possess good monodispersity (Figure S1, Supporting Information). To further investigate the detailed element composition, the mapping data acquired from high-angle annular dark-field scanning TEM (HAADF-STEM) and its energy dispersive X-ray (EDX) show that C, O, Cu, and Mo elements are all homogeneously distributed on POD-M. Meanwhile, for the virus-like V-POD-M, the Si elements can be obviously detected with the spiky silica shell showing a thickness of 130 nm (Figure 1e,f).

We performed a careful analysis of POD-M and V-POD-M with X-ray photoelectron spectroscopy (XPS), X-ray diffraction (XRD), Fourier transform infrared spectrometry (FTIR), and thermogravimetric analysis (TGA) have been performed for POD-M and V-POD-M. The XPS survey scan of POD-M gives C 1s, O 1s, Cu 2p, and Mo 3d signals (Figure S4, Supporting Information); and in high-resolution XPS C 1s spectrum, a clear curve-fitted peak at 285.8 eV is noticed (-COOH groups in BTC), illustrating the formation of the POD-M (Figures S5 and S6, Supporting Information). Compared to POD-M, the absence of Cu, Mo, and -COOH signals and the rise of Si 2s and Si 2p peaks in the XPS spectra of V-POD-M demonstrate the formation of the shell (Figure S4, Supporting Information). V-POD-M presents a similar XRD pattern to POD-M, indicating that MOFs original crystal structure is maintained after the coating of the virus-like silica shell (Figure S7, Supporting Information). The characteristic FTIR peak at 1103 cm⁻¹ corresponds to Si-O-Si stretching vibration, which also confirms the presence of the silica shell (Figure S8, Supporting Information). The zeta potential of POD-M is -26.10 mV; after synthesizing a spiky silica shell, the value increases to 3.99 mV, indicating the almost electrical neutral surface of V-POD-M (Figure S9, Supporting Information). Furthermore, the weight ratio of the virus-like silica shell is estimated to be around 7.71 wt% according to the TGA results (Figure S10, Supporting Information). The morphology and chemical structure data strongly suggest the successful synthesis of POD-M and V-POD-M.

To avoid the influence of organic molecules and silica shell, the co-catalytic effects of compounds with Cu (II)+MoO₃ centers are first investigated at a very low concentration of merely 16 μg mL⁻¹. The colorless 3,3,5,5-tetramethylbenzidine (TMB) is employed as a molecular probe, which can be converted to blue oxidized TMB (oxTMB) in the presence of PODmimics and H₂O₂ (Figure 2a). [45-47] After incubation for 20 min, negligible color changes have been observed for TMB+H2O2 and TMB+H₂O₂+MoO₃, demonstrating no peroxide catalytic activity of MoO₃. While the groups of TMB+H₂O₂+Cu (II) and TMB+H₂O₂+Cu (II)+MoO₃ both turn blue, indicating the catalytic activity of Cu (II) (Figure S11, Supporting Information). After incubation for 20 min, the TMB+H₂O₂+Cu (II)+MoO₃ group shows a strong absorbance peak at 652 nm (Figure 2b,c), indicating the formation of oxTMB. Inspired by the Fenton reaction, one possible mechanism for the catalytic process is decomposing the H₂O₂ molecules into hydroxyl radicals (•OH).[48] Therefore, terephthalic acid (TA) was used to monitor the •OH generation ability by detecting the formed 2-hydroxy TA molecule (TAOH, with unique fluorescence at 435 nm,

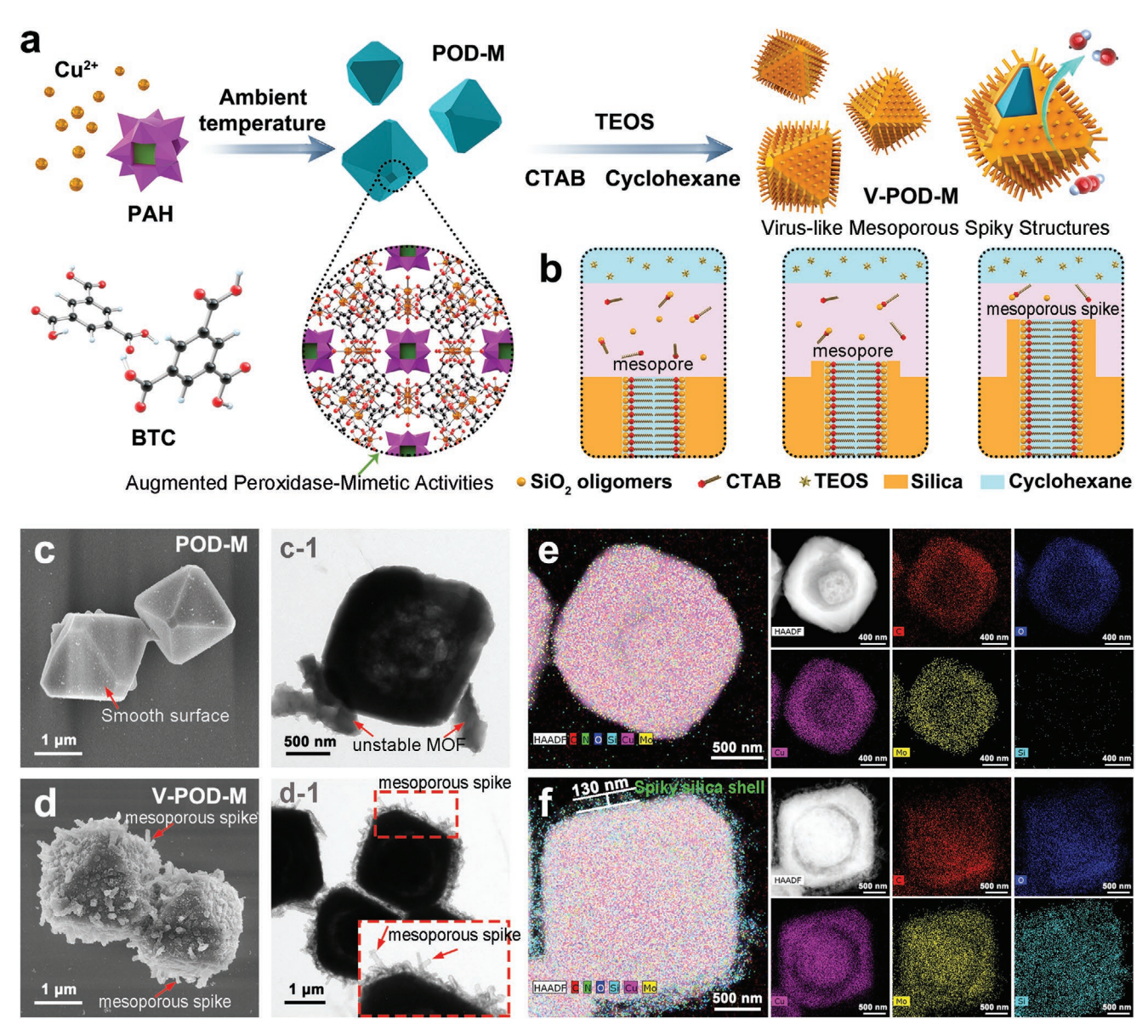


Figure 1. Synthesis and characterization of POD-M and V-POD-M. a,b) Schematic illustration for V-POD-M synthesis (a) and virus-like silica shell formation (b). c,d) High-resolution SEM images of POD-M (c) and V-POD-M (d) and TEM images of POD-M (c-1) and V-POD-M (d-1). e,f) HAADF-STEM images and EDX elemental mapping patterns of POD-M (e) and V-POD-M (f).

Figure 2d.^[49] As shown in Figure 2e,f, only the TA+ H_2O_2 +Cu (II)+ MoO_3 mixture shows an intense photoluminescence signal, which proves the ultrahigh POD-mimetic catalytic activity of Cu (II)– MoO_3 system. The above data suggest that MoO_3 cannot catalyze H_2O_2 to produce •OH, but it may serve as a cocatalyst to enhance the POD-mimetic catalytic activity of Cu (II) and accelerate •OH generation.

To further confirm the ROS species, by using free radical trapping agents, the electron paramagnetic resonance (EPR) signals of •O₂⁻ and •OH are evaluated. The intensity of •OH signal in Cu (II)+MoO₃ increases sixfold when compared with that in bare Cu (II), validating the accelerated •OH generation ability of the Cu (II)+MoO₃ system (Figure 2g). In terms of •O₂⁻ generation, there is only a slight increase for the Cu (II)+MoO₃ system when compared to bare Cu (II) (Figure S12, Supporting

Information). The EPR data suggest that the Cu (II)+MoO₃ co-catalytic system mainly increases the •OH generation, which may benefit from the high adsorption and binding ability between $\rm H_2O_2$ and $\rm MoO_3$. Based on this mechanism, we propose two main reaction pathways, including the formation of peroxo-complex-intermediate first and then Fenton-like reaction (Reaction Path 1), or direct Fenton-like reaction with Cu (II) (Reaction Path 2). Density functional theory (DFT) calculations were employed to simulate both reaction processes to generate the •OH (**Figure 3**). Through energy barrier calculation, we first demonstrate that $\rm MoO_3$ can easily absorb $\rm H_2O_2$ molecules by the nucleophilic attack (relative Gibbs free energy $\Delta G = 0.06$ eV) to produce peroxo-complex-intermediate (Figure 3a,b); the ΔG required for Cu (II) to catalyze peroxo-complex-intermediate is 0.24 eV, which is substantially lower compared with that of

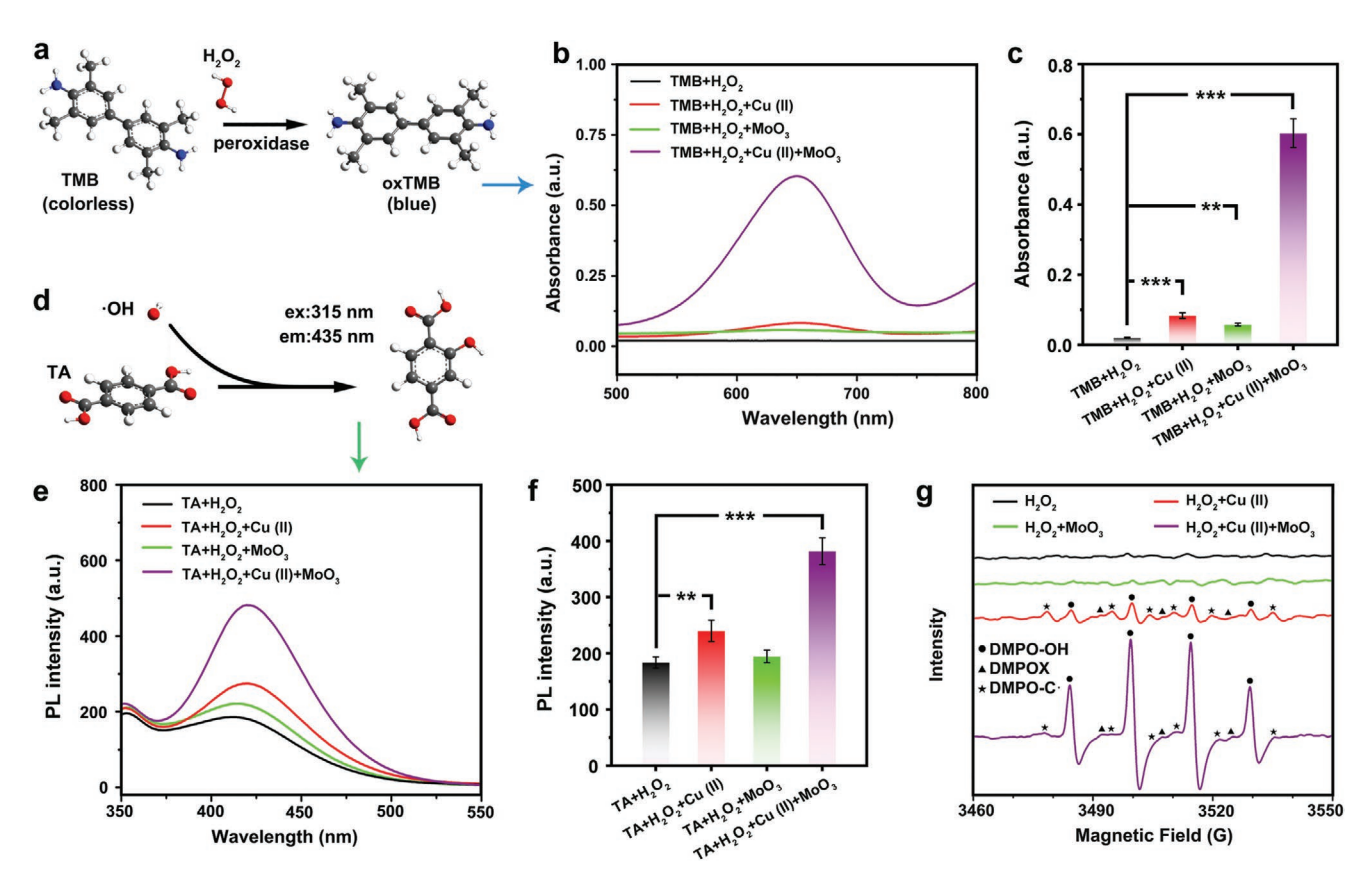


Figure 2. Synergetic POD-mimetic catalytic properties of compounds with Cu (II) and MoO₃ centers. a) Oxidation reaction of TMB. b) UV–vis absorption spectra and c) absorbance values of TMB solutions incubated with H_2O_2 , $H_2O_2+MoO_3$, H_2O_2+Cu (II), and H_2O_2+Cu (II)+MoO₃ systems for 20 min. d) Reaction mechanism of TA and •OH. e) The fluorescence spectra and f) intensity values of different samples after reacting with TA. g) EPR spectra for the detection of •OH generated from different systems. In the above experiments, 5′,5-dimethyl-1-pyrroline *N*-oxide (DMPO) is used as a free-radical trapping agent.^[50] The concentrations of H_2O_2 , MoO₃, and Cu (II) are 0.1×10^{-3} M, 16 μg mL⁻¹, and 16 μg mL⁻¹, respectively. Asterisks indicate significant differences (**P < 0.01, ***P < 0.001). All values are expressed as mean ± SD, n = 5.

using Cu (II) to catalyze H_2O_2 directly (0.38 eV) (Figure 3c–e). For the formation of •OH, the peroxo-complex-intermediate also significantly reduces the free energy when reacting with Cu (I); the required ΔG is 0.24 eV, which is much lower than that of the Cu (I)+ H_2O_2 group ($\Delta G=0.36$ eV). Therefore, we theoretically verify that the Cu (II)+ MoO_3 cocatalysts can reduce the energy barrier required for •OH generation compared to bare Cu (II) catalytic process, the formation of peroxo-complex-intermediate significantly accelerate the whole radical formation rate.

The peroxidase-mimetic catalytic performances of POD-M and V-POD-M were also systematically studied. Owing to the cocatalytic effects of Cu (II) and MoO₃, both the POD-M and V-POD-M possess ultrahigh peroxide catalytic activities at a very low concentration (16 µg mL⁻¹, Figures S13–S19, Supporting Information). The fast release of Cu (II) and MoO₃ compounds from the V-POD-M further validates the mesoporous structure of the coated spiky silica shell. The TMB and TA results and EPR spectra validate our hypothesis that the coating of spiky silica shells only has a negligible effect on the POD-mimetic catalytic performances (Figures S17–S19, Supporting Information). Besides, glutathione (GSH), playing a vital role in preventing microbe from being damaged by oxidative stress, has been utilized to evaluate the oxidization property of the

POD-M+H₂O₂ and V-POD-M+H₂O₂ systems in complex bacterial environments.^[51,52] Combined with the color rendering effect of 5,5'-dithiobis(2-nitrobenzoic acid) (DNTB) indicator, the color of GSH solutions can be changed from colorless to yellow. In contrast, the color of the oxidized GSH solutions remains unchanged. According to the above results, the highly toxic ROS generated by POD-M and V-POD-M can rapidly oxidize GSH within few seconds and destroy the microbial antioxidant system and substances, laying the foundations for efficient sterilization (Figures S20 and S21, Supporting Information).

To systematically calculate the bactericidal ratios, the viabilities of the bacteria (Gram-positive *Staphylococcus aureus* and Gram-negative *Escherichia coli*) incubated with six different systems were studied via agar plate counting and optical density values at 600 nm ($\mathrm{OD_{600}}$). Compared to the control group (819 colony-forming units, CFU, for *S. aureus* and 971 CFU for *E. coli*), similar bacterial colony numbers (795 CFU for *S. aureus* and 893 CFU for *E. coli*) are observed after incubating with $\mathrm{H_2O_2}$ (0.1×10^{-3} M), indicating that $\mathrm{H_2O_2}$ itself presents insignificant bacteriostatic activity. While the colony number of the bacteria+V-POD-M mixture (496 CFU for *S. aureus* and 602 CFU for *E. coli*) decreases more rapidly than bacteria+POD-M (673 CFU for *S. aureus* and 757 CFU for *E. coli*), demonstrating that the virus-like shell can enhance the bacteriostatic property

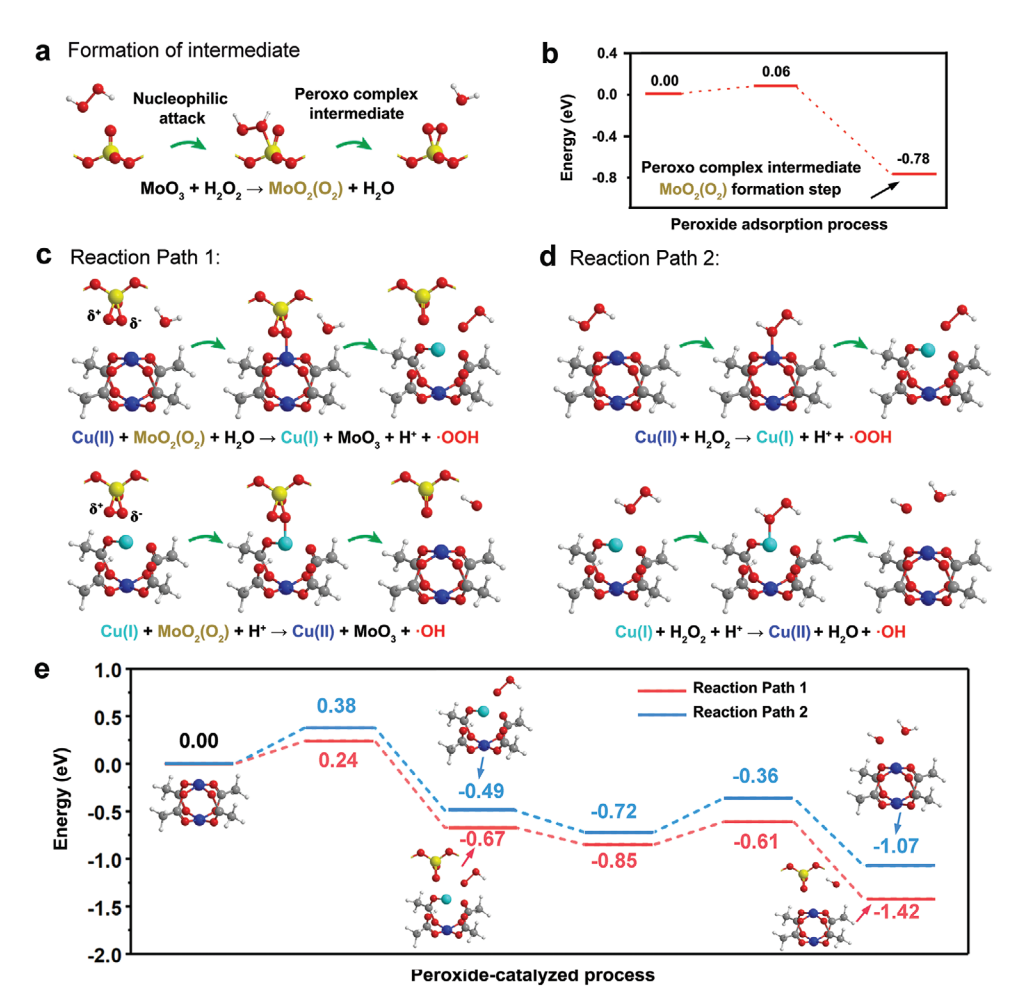


Figure 3. Theoretical calculations of peroxide catalytic activities. a) The peroxide intermediate complexation reaction between the MoO_3 and H_2O_2 , and b) corresponding Gibbs free energy diagrams. c) Theoretical calculation schematics of peroxide catalytic reaction paths of Cu (II)+ intermediate/ H_2O_2 in (a), and d) the theoretical calculation of Cu (II)/ H_2O_2 systems. e) Gibbs free energy diagrams of each reaction step in (c) and (d).

from 16% and 23% of POD-M to 39% and 40% of V-POD-M for S.~aureus and E.~coli, respectively. More importantly, V-POD-M shows nearly 100% bacterial inhibition ratios in the presence of small amounts of H_2O_2 (0.1×10^{-3} M), confirming that such accelerated peroxidase-mimetic catalytic system appending bacterial capture ability can achieve complete bacterial eradication at ultralow concentrations (16 µg mL $^{-1}$, **Figure** 4a and Figure S22, Supporting Information). The OD $_{600}$ values exhibit breeding processes of the bacteria treated with different systems; this result is consistent with that from the agar plate counting experiment (Figure 4b,c). Moreover, we further investigate the antibacterial activity of the released Cu (II) and MoO_3 when the POD-M and V-POD-M react with H_2O_2 , suggesting that the releasing substance has little effect on killing the bacteria (Figures S23 and S24, Supporting Information). [54,55]

Fluorescence microscopy images also provide visual evidence for efficient bactericidal capabilities of the V-POD-M system. As the ROS cannot be localized on the bacteria, POD- $M+H_2O_2$ with a flat surface shows the insufficient capability to eradicate the bacteria, providing certain possibilities for the regrowth of bacteria; in contrast, no live bacterium is observed in the V-POD- $M+H_2O_2$ group, which may be attributed to its

spiky silica shells (Figure 4d, and Figures S25–S27, Supporting Information). It is worth noting that the proposed LCK process has been observed for the V-POD-M+H₂O₂ group, suggesting that the virus-like structure can contribute to the bacterial capture and facilitate the localized ROS killing of bacteria. Furthermore, minimum inhibitory concentration (MIC) data show that the MIC of V-POD-M+H₂O₂ (around 16 μg mL⁻¹) is much lower than other groups for both *S. aureus* and *E. coli* (Figure 4e,f). The MBC value of the V-POD-M+H₂O₂ system is 16 μg mL⁻¹ for both *S. aureus* and *E. coli* (Figures S28 and S29, Supporting Information), demonstrating the catalytic sterilization system of V-POD-M also possesses a potent bacterial eradication ability.

To further reveal the localized and fast bacterial capture and ROS killing process of the developed V-POD-M, we subsequently investigated the process of LCK action. We assumed that V-POD-M could efficiently capture bacteria due to its virus-like tough shell. In the presence of small amounts of H_2O_2 , highly toxic •OH is promptly generated via the synergetic catalysis of V-POD-M. The •OH can directly diffuse into the captured bacteria and destroy the bacterial membrane and affect its permeability, which facilitates the intrusion of ROS, thus resulting in DNA damage (Figure 5a). The bacterial

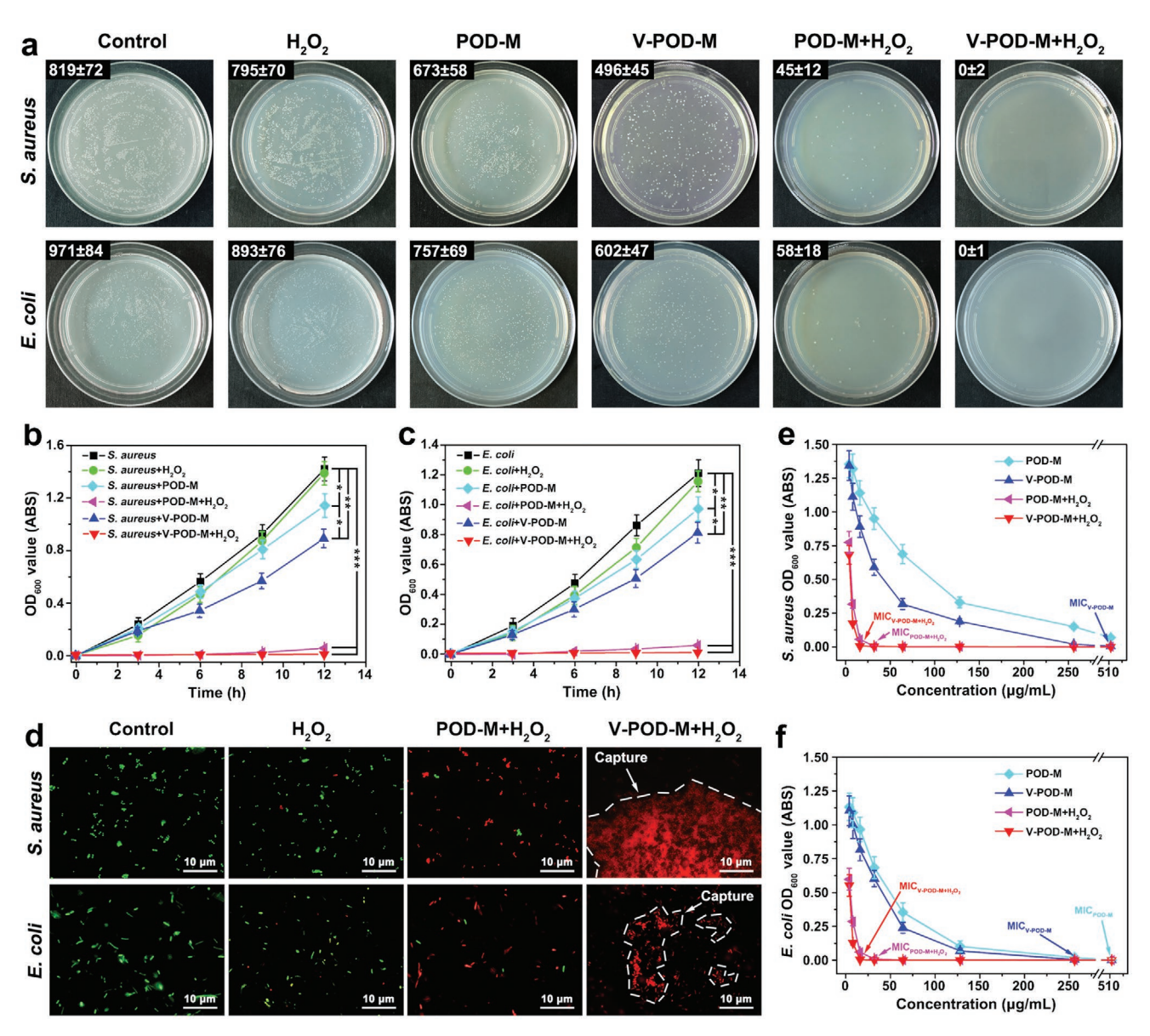


Figure 4. In vitro antibacterial properties. a) Agar plate digital photographs. b,c) OD₆₀₀ values of bare bacteria and the bacteria incubated with H_2O_2 , POD-M, V-POD-M, POD-M+ H_2O_2 , and V-POD-M+ H_2O_2 groups. d) Live/dead fluorescence images of bare bacteria and the bacteria treated with H_2O_2 , POD-M+ H_2O_2 , and V-POD-M+ H_2O_2 groups. e,f) MIC values of POD-M, V-POD-M, POD-M+ H_2O_2 , and V-POD-M+ H_2O_2 . All values are expressed as mean \pm SD, n = 5. *P < 0.05, **P < 0.01, ***P < 0.001.

sections and high-resolution TEM imaging results were further investigated to validate the irreversible damage caused by this LCK action visually. After incubation with V-POD-M, it is observed that the spikes on the surface of V-POD-M can easily penetrate the bacterial cytomembranes and firmly capture the bacteria (marked by blue arrows); after incubation with V-POD-M+H₂O₂, the bacterial cytomembranes become fragmentary (marked by red arrows), indicating the robust bacterial capture and eradication ability of V-POD-M+H₂O₂ (Figure 5b and Figure S30, Supporting Information). From the SEM image of different groups, the bare H_2O_2 (0.1×10^{-3} M) incubated bacteria show good structural integrity as shown in Figure S31, Supporting Information. For the POD-M+H₂O₂ group, as shown in Figure 5c, most of the bacteria are not damaged, which

reveals that the produced nonlocalized ROS exhibits limited antibacterial activities. Once incubated with V-POD-M+ H_2O_2 , the bacterial morphology has visible deformation and collapse, demonstrating that the in situ ROS production can severely destruct the captured bacteria. Therefore, the efficient bacterial capture abilities will endow the V-POD-M with a satisfied bactericidal performance even at a very low concentration.

We have observed the obvious LCK action of the V-POD-M in the study present above; however, the detailed mechanisms of capture and strong adhesion between bacteria and virus-like V-POD-M are not revealed. As reported in earlier literature, [56,57] bacteria are inclined to adhere to rough surfaces; thus, the interactions between bacteria and the virus-like rough surface of V-POD-M are further analyzed by molecular dynamics (MD)

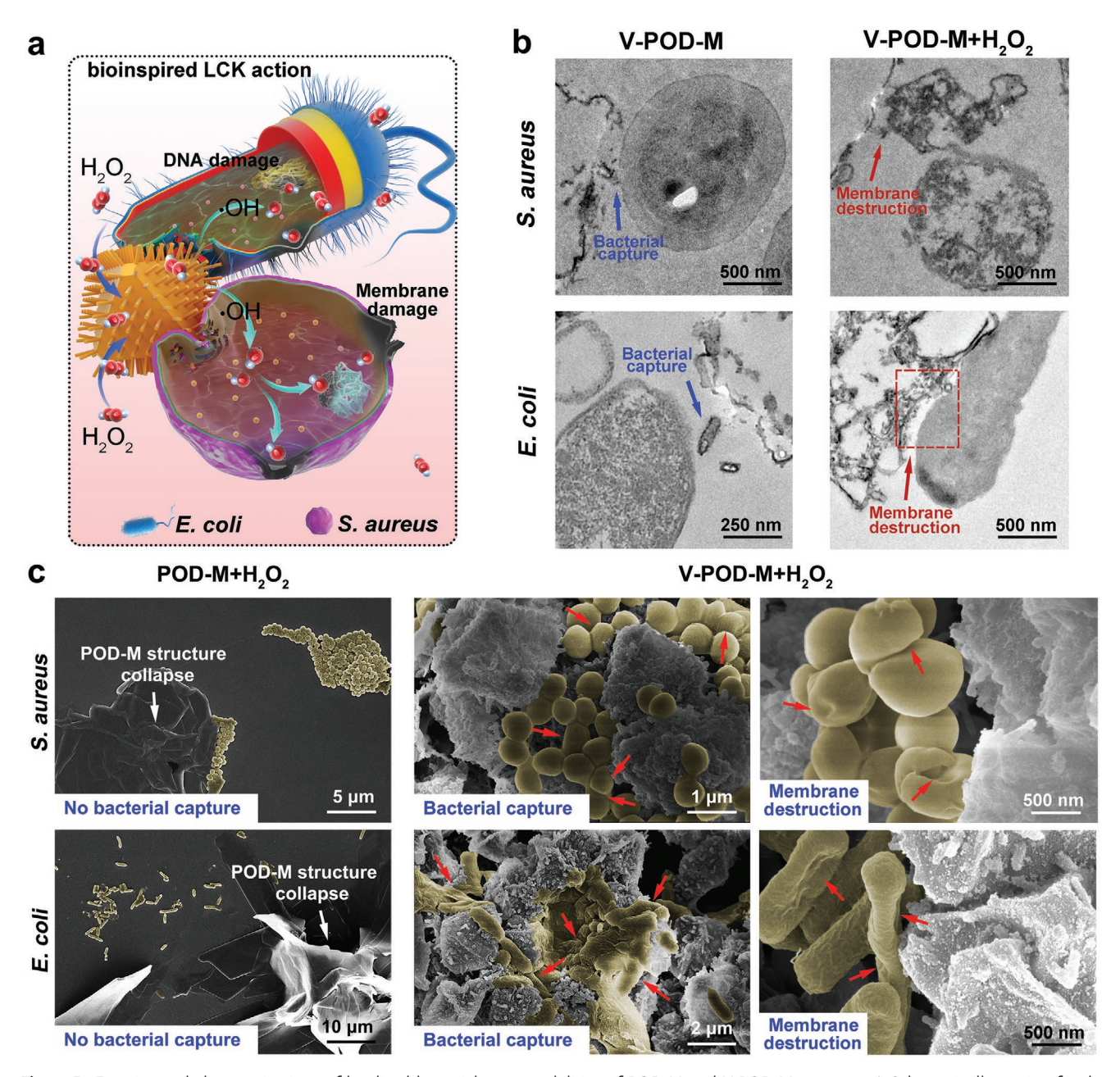


Figure 5. Experimental characterizations of localized bacterial capture abilities of POD-M and V-POD-M systems. a) Schematic illustration for the LCK action-based antibacterial mechanism of V-POD-M. b) TEM images of bacterial sections after V-POD-M and V-POD-M+ H_2O_2 incubation. c) SEM images of the bacteria incubated with POD-M+ H_2O_2 and V-POD-M+ H_2O_2 . The morphologies of destroyed bacterial cytomembranes are marked by the red arrows.

simulations.^[58] It should be noted that the real interactions between bacterial membranes and nanostructures are very complex. To simplify the calculation model, we first create a penetration simulation model using the cytomembrane surrounded by H₂O molecules and nanostructures with a flat surface (size: 12.53 nm ×12.53 nm) and epitaxial nanotubes-based spiky surface (diameter: 1.43 nm), respectively. And then, pulling force is introduced to enable the surfaces to move towards the lipid bilayer in the simulation process (Figures S32–S34, Supporting Information). In the actual process, the pulling force mainly corresponds to the collision between nanomaterials and

bacteria caused by the physical vibration and mixing from the shaker and also the Brownian motion and van der Waals force. During the penetration process, the flat surface is incapable of intruding into the membrane, and the bilayer keeps its initial integrity structure. In contrast, the spiky nanotubes on the virus-like surface can readily impale the membrane, and the typical bilayer structure is gradually destroyed (**Figure 6**a,b). These distinct processes are quantified by monitoring the center of the mass distance between the membrane and the surfaces. The two different surfaces can contact the exterior of the membrane within 6 ns. After that, the distance of the flat surface

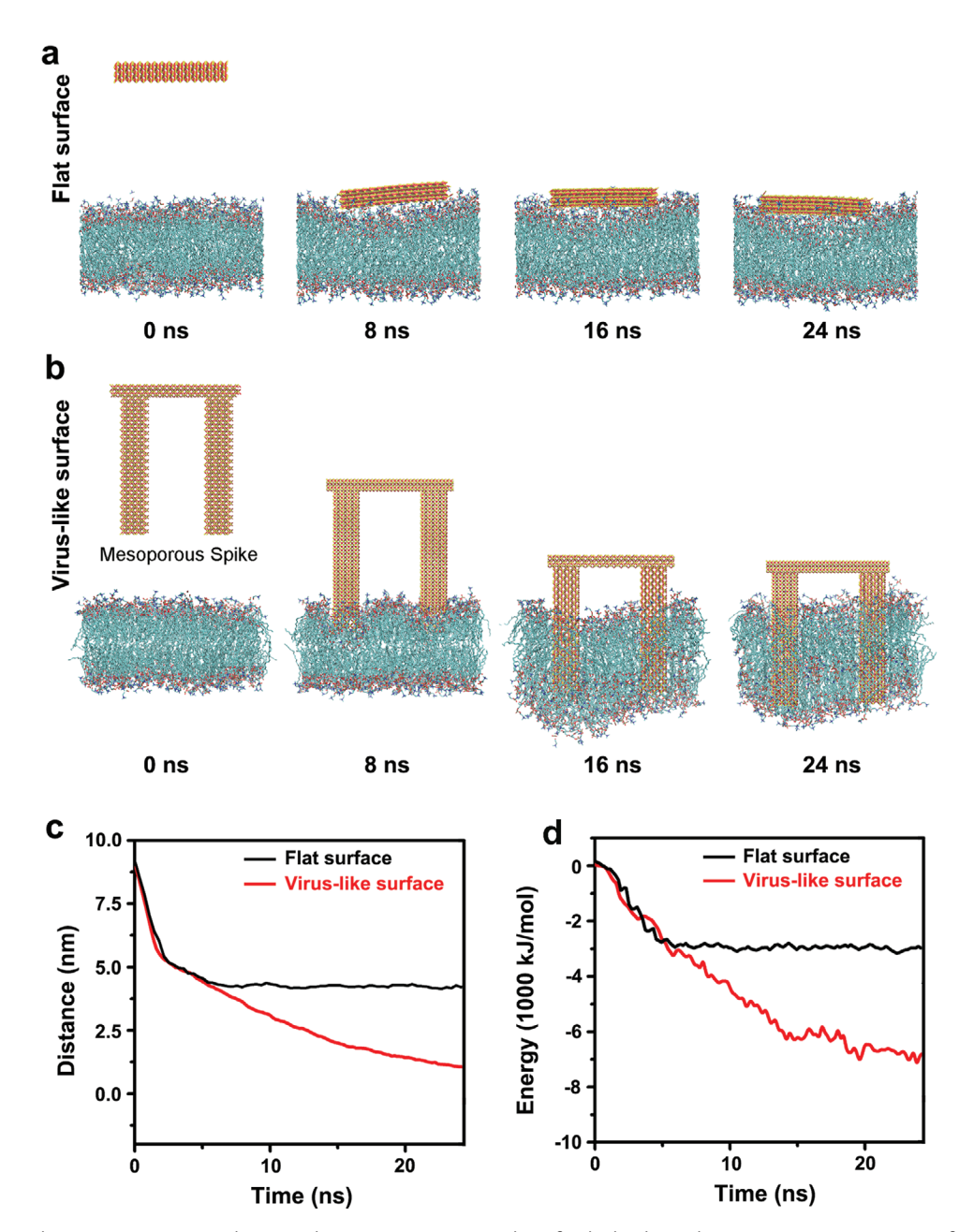


Figure 6. Lipid membrane penetration simulations. a,b) Representative snapshots for the lipid membrane penetration processes of a flat silica surface (a) and a virus-like silica-shell surface (b). c) Time evolution of the center of the mass distance between the membrane and two different surfaces. d) Time evolution of the interaction energy between the lipid membrane and two different surfaces.

almost remains constant. The situation is completely different for the virus-like surface that reaches deeper into the interior of the membrane. Even after 25 ns, the distance curve still does not reach a plateau level, validating the efficient bacterial membrane piercing ability of our virus-like surface (Figure 6c).

We further observe the intrusion event by analyzing the time evolution of the interaction energy between the lipid membrane and flat/spiky surface (Figure 6d). At 15 ns, the interaction energy of virus-like spiky surface increased to \approx -6500 kJ mol⁻¹, which is much larger than that of the flat surface (\approx -3000 kJ mol⁻¹). Meanwhile, after 25 ns, the interacting curve still does not reach a plateau, and thus, favoring

the idea that the penetration process can continue for V-POD-M if given enough time. Meanwhile, the flat surface reaches a plateau only after 5 ns, thus demonstrating the strong interaction between bacterial membrane and the spiky surface. Thereby, we demonstrate that the spiky V-POD-M can easily adhere to bacterial membranes compared to the flat POD-M, providing much higher possibilities for V-POD-M to capture bacteria firmly.

Before animal experiments, the cellular compatibility of V-POD-M is first investigated (Figures S35 and S36, Supporting Information). The results demonstrate that the damage caused by V-POD-M+ H_2O_2 to mammal cells is reversible, and for

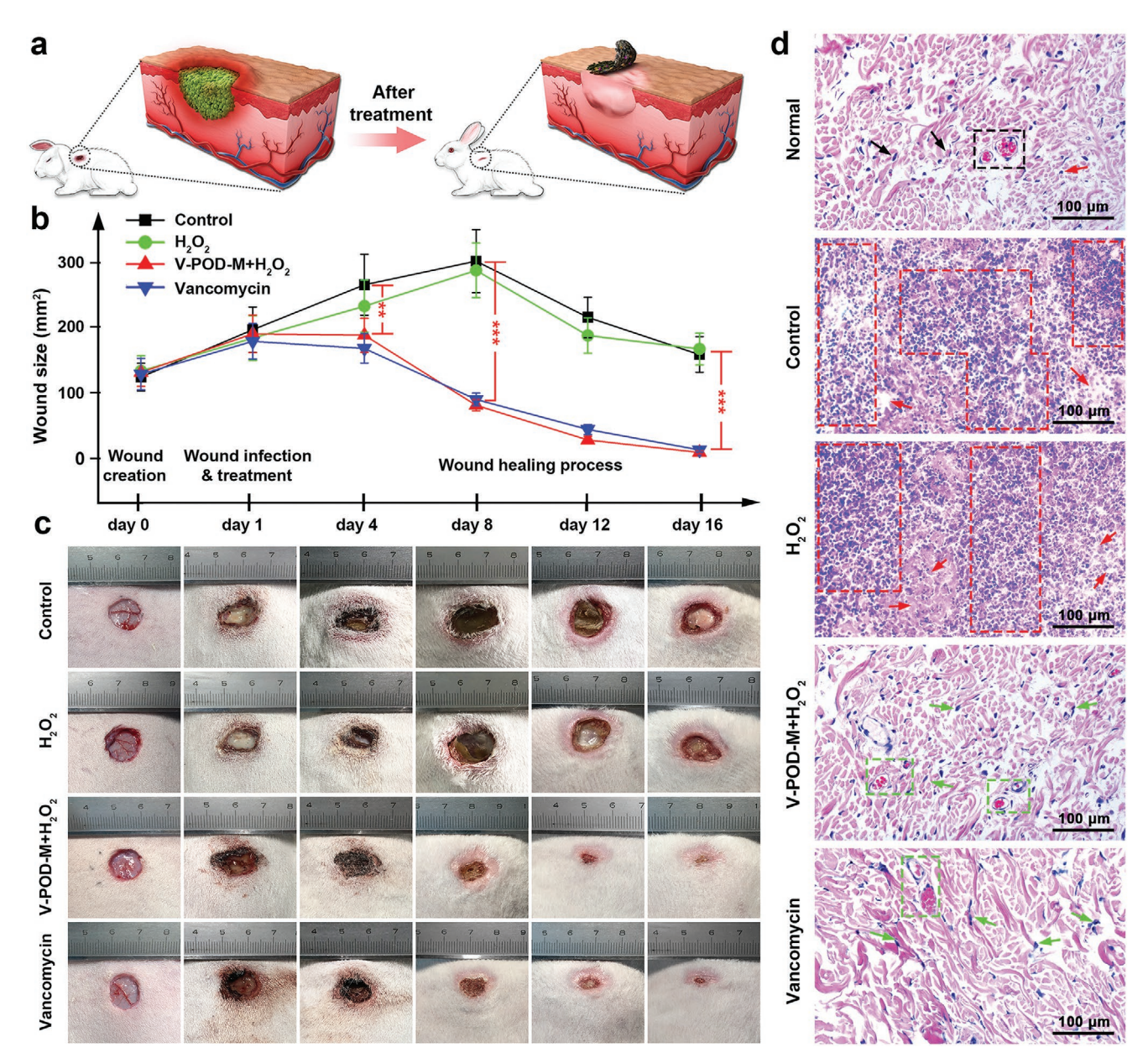


Figure 7. In vivo wounds disinfection abilities of V-POD-M and antibiotic. a) Schematic illustration for the wound disinfection and healing process. b) Time evolution of the sizes of the wounds treated by different systems. c) Digital photographs of the wounds' construction, infection, disinfection, and healing. d) H&E staining images of the epidermal histological sections in different groups after 16 days' posttreatment. Asterisks indicate significant differences (**P < 0.01, ***P < 0.001). All values are expressed as mean \pm SD, n = 5.

long-term culture, such a system is safe to the normal tissue cells. We performed animal wound disinfection and healing experiments to further validate the potential feasibility of V-POD-M+H₂O₂ as an antibiotic-free treatment. The wound infection model of rabbits' epidermal tissue is first established by skin removal and introduction of *S. aureus* (dose: 100 μ L, concentration: 1×10^8 CFU mL $^{-1}$). At 1 d postintroduction of bacteria, a severely infected wound can be observed, and then, the LCK action of V-POD-M+H₂O₂ is utilized for short-term treatment. After the anti-infection treatment, the pyogenic wound gradually recovers, and the epidermal tissue promptly regenerates (**Figure 7**a).

Moreover, in this animal experiment, H_2O_2 (0.1 \times 10⁻³ M) group has been designed to show the excellent efficacy of the V-POD-M+ H_2O_2 group, and the POD-M+ H_2O_2 group has also been set to compare with the V-POD-M+ H_2O_2 group. In contrast, vancomycin (16 μ g mL⁻¹) has been employed to mimic traditional antibiotic treatment whose MIC value is around 4 μ g mL⁻¹ (Figure S37, Supporting Information). The entire wound healing process was captured by digital photography that allowed recording the size of wounds at different periods (Figure 7b,c and Figure S38, Supporting Information). It is clearly observed that on day 1 the infected wounds are all filled with sanies and surrounded by the inflamed epidermis,





www.advmat.de

demonstrating the successful infection of S. aureus. On day 8, the normal saline- and H₂O₂-treated wounds become worse; in contrast, the wounds treated by V-POD-M+H₂O₂ and vancomycin quickly scab and show reduced swelling. After 16 d, wounds in the control and H2O2 groups still release sanies, and in the POD-M+H₂O₂ group show a smaller scab, whereas the wounds in the V-POD-M+H2O2 and vancomycin groups are almost healed. The sizes of the scars on different days are also calculated to monitor the healing state. After normal saline and H₂O₂ treatments, the infected wounds gradually expand to more than double the initial size and subsequently recover at a prolonged rate. For the V-POD-M+H₂O₂ and vancomycin groups, the wounds present no expansion tendency and are completely repaired within 15 d (Figure 7c), preliminarily illustrating that, in the presence of small amounts of H₂O₂ $(0.1 \times 10^{-3} \text{ m})$, the V-POD-M with catalytic LCK action possesses superb wound disinfection performance even at a very low concentration (16 µg mL⁻¹) and its therapeutic effect is at a similar level to vancomycin.

Furthermore, after the treatments with different systems, the precise bacterial amounts on these wounds are monitored. The bacterial counting results show that H2O2 at low concentrations has no disinfection ability, and POD-M+H2O2 exhibits limited bacterial killing efficiency, but the V-POD-M+H₂O₂ can thoroughly eradicate the live bacteria on the wound, which is comparable to the sterilization ability of vancomycin (Figure S39, Supporting Information). To investigate the infection state of wounds, pathological analysis of histological sections is also performed via hematoxylin and eosin (H&E) staining. Compared with the healthy epidermis (marked by black arrows and rectangle), the tissue in the control and H₂O₂ groups emerge large areas of necrotic polymorphonuclear leukocytes (marked by red rectangles) and fragmentary cells (marked by red arrows); meanwhile, the collagen fibrils in intercellular substance also show disordered texture, representing the characteristics of severe wound infection. However, after posttreatment by V-POD-M+H₂O₂, typical areas of inflammation vanished at day 16, and the regeneration of abundant dermal fibroblasts (marked by green arrows) and neovascularization (marked by green rectangles) are noticed, verifying the rapid and effective wound disinfection ability of V-POD-M+H2O2. Besides, no obvious foreign-body response or accumulation of V-POD-M is observed in the new epidermal tissue. More importantly, the wound treated with vancomycin exhibits similar pathological features to those treated with V-POD-M+H₂O₂, thus guaranteeing the promising applications of the V-POD-M+H₂O₂ system in antibiotics-free treatment. Furthermore, the main organs of the rabbits are examined by H&E staining (Figure S40, Supporting Information), and no apparent damage or abnormalities are found in these tissue slices, indicating the biosafety of V-POD-M+H₂O₂-based disinfection therapy.

Furthermore, to investigate the recovery ability in the infected wound, we have performed the pathological and immuno-fluorescence analysis. Masson staining is used to evaluate the healing progress (**Figure 8**a and Figure S41, Supporting Information). The wound epidermis of the POD-M+H₂O₂, V-POD-M+H₂O₂, and vancomycin groups are similar to the normal skin tissue, while the epidermis of the control and H₂O₂ groups are uneven and thickened due to the parakeratosis, epidermal

hyperplasia, and inflammatory infiltration. We further analyze the epidermal thickness index as shown in Figure 8c. On the 16th day, the indexes of the control (8.03 \pm 1.20) and H_2O_2 (7.01 \pm 1.14) groups are very high. Though the POD-M+H $_2O_2$ group (3.99 \pm 0.71) exhibits an apparently decreased index, which is still higher than that of the V-POD-M+H $_2O_2$ (1.96 \pm 0.31) and vancomycin (2.26 \pm 0.25) treated groups. Moreover, the collagen fibers could also be proved by Masson staining (Figure S41, Supporting Information). After 16 d of treatment, the wounds of the V-POD-M+H $_2O_2$ and vancomycin treated groups exhibited well-established collagen fibers and dermal layers.

The formation of new capillaries usually accompanies the wound healing process. With the aid of the CD31 staining, the endothelial cells could be marked to reflect newly formed vessels after the revascularization of the wound area. As shown in Figure 8b, confocal laser scanning microscope reconstructs the 3D revascularization process by immunofluorescence staining of CD31. Few CD31-positive cells were found in the control and H_2O_2 groups whose expressions are 35.62 \pm 5.23% and 41.71 \pm 7.23%. The POD-M+H₂O₂ treated one shows increased CD31 expression (70.18 \pm 4.15%). The V-POD-M+H₂O₂ and vancomycin groups exhibit further increased CD31 positive cells and CD31 expressions for 75.47 \pm 5.26% and 77.52 \pm 4.23%, respectively, thus demonstrating better-wound healing compared to the POD-M+H₂O₂. As shown in Figure 8e, the V-POD-M+H₂O₂ $(57 \pm 5 \text{ vessels mm}^{-2})$ and vancomycin $(58 \pm 3 \text{ vessels mm}^{-2})$ treated groups show the highest number of new capillaries, indicating better-wound healing compared with control (27 \pm 4 vessels mm⁻²) and H_2O_2 (33 ± 6 vessels mm⁻²) groups. Besides, the immunohistochemical staining of CD31 also gives similar results (Figure S42, Supporting Information). These data demonstrate that the V-POD-M system could effectively eradicate the bacteria at the in vivo wound site, thus leading to better wound recovery ability.

In summary, by mimicking the bacteriophage-inspired LCK action, we have developed a virus-like peroxidase-mimic with synergistic ROS catalysis and efficient bacterial capture. This innovative endeavor contributes to an outstanding possibility to develop efficient disinfection strategies to replace conventional clinical antibiotic treatments. The experimental results and DFT calculations show that the loaded MoO₃ in MOFs can serve as peroxo-complex-intermediate to accelerate the Fenton-like catalytic activities of Cu (II) component, which significantly facilitates the •OH radical generation reaction. The electron microscopy and MD simulation results suggest that the virus-like V-POD-M can strongly interact with the bacterial membrane, thus facilely capturing bacteria to achieve localized bacterial killing.

In general, for antibacterial therapy, we think it is essential to balance the toxicity to cells/tissues (dosage as low as possible) and the thorough eradication of bacteria (no live bacteria). Therefore, our virus-like peroxidase-mimics system possesses thorough eradication to bacteria with limited toxicity toward wound tissue, which guarantees its future potential applications in clinical disinfection. Overall, the integrated unique virus-like mesoporous spikes and high ROS catalytic activity endow the V-POD-M with rapid bacterial capture and a high killing ratio. Thereby, in the presence of small amounts of $\rm H_2O_2$ (0.1 × 10⁻³ M), the V-POD-M possesses efficient disinfection performance (nearly 100%) for both in vivo and in vitro at very low

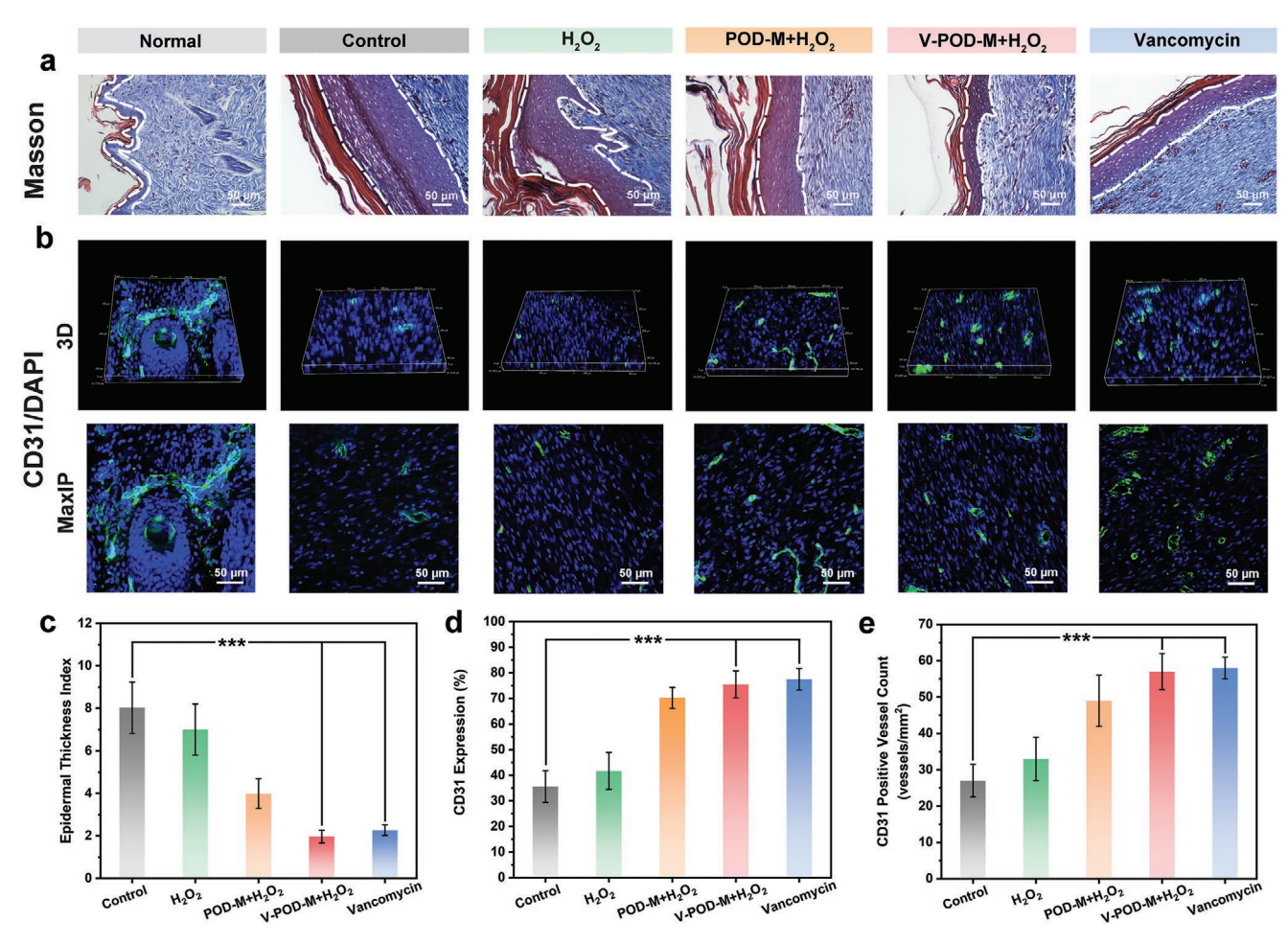


Figure 8. Pathological and immunofluorescence analysis of wounds recovery abilities. a) Masson staining images of the epidermal histological sections (the section between the white dash lines: epidermis layer). b) CD31/DAPI staining images of 3D reconstruction and corresponding maximum intensity projection (MaxIP). c) Epidermal thickness index $(\delta_1/\delta_2, \delta_1$: the average thickness of the wound epidermal layer; δ_2 : the average thickness of the normal epidermal layer). The index value is closer to 1 indicates that the epidermal layer is closer to normal skin, n = 5. d) The CD31 expression ratio of the wound tissues. e) Number of CD31 positive vessels. Data is from at least five fluorescent images. Asterisks indicate significant differences (**P < 0.01, ***P < 0.001). All data are acquired from the rabbits' wound tissues in different groups after 16 days' post-treatment. All values are expressed as mean \pm SD, n = 5.

concentrations (16 µg mL⁻¹), which is similar to the treatment and recovery efficiency of vancomycin. This inexpensive, durable, and highly ROS catalytic active V-POD-M with LCK action will not only provide a promising broad-spectrum therapy for non-antibiotic disinfections but also show enormous possibilities to serve as antibacterial nanoagents for implantable devices, composite scaffolds, and many other biomedical applications.

Experimental Section

Experimental details, including materials, characterizations, synthesis of V-POD-M, biocompatibility, peroxidase-mimic catalytic assays, in vitro and in vivo antibacterial experiments, DFT calculations, and MD simulations, are listed in the Supporting Information.

Supporting Information

Supporting Information is available from the Wiley Online Library or from the author.

Acknowledgements

This work was financially supported by the National Key R&D Program of China (2019YFA0110600, 2019YFA0110601, 2016YFC1103001, and 2016YFC1103000), National Natural Science Foundation of China (Nos. 82071938, 82001824, 82001829, 51903178, 81971622, 51803134, and 51703141), the Science and Technology Project of Sichuan Province (Nos. 2020YFH0087, 18YYJC1417, 2019YFS0219, and 2020YJ0055), Special Funds for Prevention and Control of COVID-19 of Sichuan University (2020scunCoV-YJ-20005) and SKLFPM, Donghua University (YJ202005). C.C. acknowledges the support of the State Key Laboratory of Polymer Materials Engineering (No. sklpme2019-2-03), Fundamental Research Funds for the Central Universities, Thousand Youth Talents Plan, and Alexander von Humboldt Fellowship. The authors thank Zhongkebaice Technology Service Co. Ltd. for TEM tests and Ceshigo for the technical support on theoretical calculations. The authors also thank their laboratory members for their generous help and gratefully acknowledge the help of Dr. Mi Zhou, Dr. Xi Xiang, Dr. Yuanjiao Tang, Ms. Xijing Yang, and Ms. Zhen Yang at Sichuan University. The authors also thank Li Li, Fei Chen, and Chunjuan Bao of the Institute of Clinical Pathology, Sichuan University for processing the histological staining. R.D.R. thanks the Tomsk Polytechnic University enhancement program 5-100. All the



ADVANCED MATERIALS

www.advmat.de

experiments involving animals in this work were approved (No. 2019001A) and followed the animal ethical standards set by the Animal Ethics Committee in West China Hospital, Sichuan University, Chengdu, China.

Conflict of Interest

The authors declare no conflict of interest.

Author Contributions

Y.Y. and X.Z.W. contributed equally to this work. Y.Y., C.S.Z., L.Q., and C.C. conceived the idea and designed the project. Y.Y., X.Z.W., L.M., C.H., and J.B.H. performed the experiments and analyzed the results. X.Z.W., S.J.C., and Y.P.L. assisted with the figure production and experiment design. Y.Y., S.J.C., R.D.R., and C.C. design and conduct the theoretical calculation. Y.Y., X.Z.W., R.D.R., C.S.Z., C.C., and L.Q. wrote and edited the manuscript. C.C., C.S.Z., and L.Q. supervised the whole project. All authors discussed the results and commented on the manuscript.

Data Availability

The authors declare that the data supporting the findings of this study are available within the paper and the Supporting Information, or are available from the authors upon request.

Keywords

bacterial capture, catalytic ROS generation, peroxidase-mimics and biomimetics, virus-like nanostructures, wound disinfection

Received: August 12, 2020 Revised: December 18, 2020 Published online:

- T. Charalampous, G. L. Kay, H. Richardson, A. Aydin, R. Baldan, C. Jeanes, D. Rae, S. Grundy, D. J. Turner, J. Wain, *Nat. Biotechnol.* 2019, 37, 783.
- [2] W. Kim, W. Zhu, G. L. Hendricks, D. Van Tyne, A. D. Steele, C. E. Keohane, N. Fricke, A. L. Conery, S. Shen, W. Pan, *Nature* 2018, 556, 103.
- [3] D. Mao, F. Hu, S. Ji, W. Wu, D. Ding, D. Kong, B. Liu, Adv. Mater. 2018, 30, 1706831.
- [4] R. Joseph, A. Naugolny, M. Feldman, I. M. Herzog, M. Fridman, Y. Cohen, J. Am. Chem. Soc. 2016, 138, 754.
- [5] M. Czuban, M. Kulka, L. Wang, A. Koliszak, K. Achazi, C. Schlaich, I. Donskyi, M. Di Luca, J. Oneto, M. Royzen, R. Haag, A. Trampuz, Mater. Sci. Eng., C 2020, 116, 111109.
- [6] J. Xue, M. He, H. Liu, Y. Niu, A. Crawford, P. D. Coates, D. Chen, R. Shi, L. Zhang, Biomaterials 2014, 35, 9395.
- [7] J. Xue, Y. Niu, M. Gong, R. Shi, D. Chen, L. Zhang, Y. Lvov, ACS Nano 2015, 9, 1600.
- [8] X. Zhang, G. Chen, Y. Liu, L. Sun, L. Sun, Y. Zhao, ACS Nano 2020, 14, 5901.
- [9] J. Qu, X. Zhao, Y. Liang, T. Zhang, P. X. Ma, B. Guo, Biomaterials 2018, 183, 185.
- [10] D. Hu, H. Li, B. Wang, Z. Ye, W. Lei, F. Jia, Q. Jin, K.-F. Ren, J. Ji, ACS Nano 2017, 11, 9330.
- [11] C. Nie, M. Stadtmüller, H. Yang, Y. Xia, T. Wolff, C. Cheng, R. Haag, Nano Lett. 2020, 20, 5367.

- [12] G. Huang, T. W. Ng, T. An, G. Li, B. Wang, D. Wu, H. Y. Yip, H. Zhao, P. K. Wong, Water Res. 2017, 118, 104.
- [13] J. Zhou, C. Wang, A. J. Cunningham, Z. Hu, H. Xiang, B. Sun, W. Zuo, M. Zhu, *Mater. Sci. Eng.*, C 2019, 101, 499.
- [14] F. Cao, L. Zhang, H. Wang, Y. You, Y. Wang, N. Gao, J. Ren, X. Qu, Angew. Chem., Int. Ed. 2019, 58, 16236.
- [15] X. Liu, Z. Yan, Y. Zhang, Z. Liu, Y. Sun, J. Ren, X. Qu, ACS Nano 2019, 13, 5222.
- [16] Y. Wang, H. Hua, W. Li, R. Wang, X. Jiang, M. Zhu, J. Dent. 2019, 80, 23.
- [17] J. Zhou, X. Fei, C. Li, S. Yu, Z. Hu, H. Xiang, B. Sun, M. Zhu, Polymers 2019, 11, 113.
- [18] L. Zheng, J. Li, M. Yu, W. Jia, S. Duan, D. Cao, X. Ding, B. Yu, X. Zhang, F.-J. Xu, J. Am. Chem. Soc. 2020, 142, 20257.
- [19] Z. Chen, Z. Wang, J. Ren, X. Qu, Acc. Chem. Res. 2018, 51, 789.
- [20] F. Cao, L. Zhang, Y. You, L. Zheng, J. Ren, X. Qu, Angew. Chem., Int. Ed. 2020, 132, 5146.
- [21] L. Ma, F. Jiang, X. Fan, L. Wang, C. He, M. Zhou, S. Li, H. Luo, C. Cheng, L. Qiu, Adv. Mater. 2020, 32, 2003065.
- [22] H. Wang, P. Li, D. Yu, Y. Zhang, Z. Wang, C. Liu, H. Qiu, Z. Liu, J. Ren, X. Qu, Nano Lett. 2019, 19, 9173.
- [23] Z. Wang, Y. Zhang, E. Ju, Z. Liu, F. Cao, Z. Chen, J. Ren, X. Qu, Nat. Commun. 2018, 9, 3334.
- [24] Q. Wu, Z. He, X. Wang, Q. Zhang, Q. Wei, S. Ma, C. Ma, J. Li, Q. Wang, Nat. Commun. 2019, 10, 240.
- [25] Z. Xu, Z. Qiu, Q. Liu, Y. Huang, D. Li, X. Shen, K. Fan, J. Xi, Y. Gu, Y. Tang, J. Jiang, J. Xu, J. He, X. Gao, Y. Liu, H. Koo, X. Yan, L. Gao, Nat. Commun. 2018, 9, 3713.
- [26] X. Zhong, X. Wang, L. Cheng, Y. a. Tang, G. Zhan, F. Gong, R. Zhang, J. Hu, Z. Liu, X. Yang, Adv. Funct. Mater. 2019, 30, 1907954.
- [27] Q. Tang, S. Cao, T. Ma, X. Xiang, H. Luo, P. Borovskikh, R. D. Rodriguez, Q. Guo, L. Qiu, C. Cheng, Adv. Funct. Mater. 2021, 31, 2007475.
- [28] Z. Tian, J. Li, Z. Zhang, W. Gao, X. Zhou, Y. Qu, Biomaterials 2015, 59, 116.
- [29] L. Huang, J. Chen, L. Gan, J. Wang, S. Dong, Sci. Adv. 2019, 5, eaav5490.
- [30] J. Wu, X. Wang, Q. Wang, Z. Lou, S. Li, Y. Zhu, L. Qin, H. Wei, Chem. Soc. Rev. 2019, 48, 1004.
- [31] B. Yang, Y. Chen, J. Shi, Adv. Mater. 2019, 31, 1901778.
- [32] X. Fan, F. Yang, J. Huang, Y. Yang, C. Nie, W. Zhao, L. Ma, C. Cheng, C. Zhao, R. Haag, *Nano Lett.* **2019**, *19*, 5885.
- [33] C. Yang, M. Zhou, C. He, Y. Gao, S. Li, X. Fan, Y. Lin, F. Cheng, P. Zhu, C. Cheng, *Nano-Micro Lett* **2019**, *11*, 87.
- [34] W. Shao, C. He, M. Zhou, C. Yang, Y. Gao, S. Li, L. Ma, L. Qiu, C. Cheng, C. Zhao, J. Mater. Chem. A 2020, 8, 3168.
- [35] C. Cheng, S. Li, Y. Xia, L. Ma, C. Nie, C. Roth, A. Thomas, R. Haag, Adv. Mater. 2018, 30, 1802669.
- [36] H. Xiang, W. Feng, Y. Chen, Adv. Mater. 2020, 32, 1905994.
- [37] Y. Gao, C. Yang, M. Zhou, C. He, S. Cao, Y. Long, S. Li, Y. Lin, P. Zhu, C. Cheng, Small 2020, 16, 2005060.
- [38] M. Masarwa, H. Cohen, D. Meyerstein, D. L. Hickman, A. Bakac, J. H. Espenson, J. Am. Chem. Soc. 1988, 110, 4293.
- [39] T. T. Nguyen, H.-J. Park, J. Y. Kim, H.-E. Kim, H. Lee, J. Yoon, C. Lee, Environ. Sci. Technol. 2013, 47, 13661.
- [40] J. Xi, G. Wei, L. An, Z. Xu, Z. Xu, L. Fan, L. Gao, Nano Lett. 2019, 19, 7645.
- [41] B. Sels, D. D. Vos, M. Buntinx, F. Pierard, A. Kirsch-De Mesmaeker, P. Jacobs, *Nature* 1999, 400, 855.
- [42] B. F. Sels, D. E. De Vos, P. J. Grobet, F. Pierard, F. Kirsch-De Mesmaeker, P. A. Jacobs, J. Phys. Chem. B 1999, 103, 11114.
- [43] M. Xing, W. Xu, C. Dong, Y. Bai, J. Zeng, Y. Zhou, J. Zhang, Y. Yin, Chem 2018, 4, 1359.
- [44] H. B. Wu, B. Y. Xia, L. Yu, X.-Y. Yu, X. W. D. Lou, Nat. Commun. 2015, 6, 6512.





www.advmat.de

- [45] S. Gao, H. Lin, H. Zhang, H. Yao, Y. Chen, J. Shi, Adv. Sci. 2019, 6, 1801733.
- [46] Z. Dong, L. Feng, Y. Hao, Q. Li, M. Chen, Z. Yang, H. Zhao, Z. Liu, Chem 2020, 6, 1391.
- [47] B. Yang, Y. Chen, J. Shi, Chem 2018, 4, 1284.
- [48] Y. Jv, B. Li, R. Cao, Chem. Commun. 2010, 46, 8017.
- [49] S. Ge, F. Liu, W. Liu, M. Yan, X. Song, J. Yu, Chem. Commun. 2014, 50, 475.
- [50] X. Pan, L. Bai, H. Wang, Q. Wu, H. Wang, S. Liu, B. Xu, X. Shi, H. Liu, Adv. Mater. 2018, 30, 1800180.
- [51] W. Yin, J. Yu, F. Lv, L. Yan, L. R. Zheng, Z. Gu, Y. Zhao, ACS Nano 2016, 10, 11000.
- [52] X. Liu, S. Sen, J. Liu, I. Kulaots, D. Geohegan, A. Kane, A. A. Puretzky, C. M. Rouleau, K. L. More, G. T. R. Palmore, Small 2011, 7, 2775.

- [53] Y. Yang, Y. Deng, J. Huang, X. Fan, C. Cheng, C. Nie, L. Ma, W. Zhao, C. Zhao, Adv. Funct. Mater. 2019, 29, 1900143.
- [54] L. P. Arendsen, R. Thakar, A. H. Sultan, Clin. Microbiol. Rev. 2019, 32, e00125.
- [55] A. M. Ribeiro, T. H. S. Flores-Sahagun, R. C. Paredes, J. Mater. Sci. 2016, 51, 2806.
- [56] W. Wang, P. Wang, X. Tang, A. A. Elzatahry, S. Wang, D. Al-Dahyan, M. Zhao, C. Yao, C.-T. Hung, X. Zhu, ACS Cent. Sci. 2017, 3, 839
- [57] H. Song, Y. A. Nor, M. Yu, Y. Yang, J. Zhang, H. Zhang, C. Xu, N. Mitter, C. Yu, J. Am. Chem. Soc. 2016, 138, 6455.
- [58] Y. Chong, X. Dai, G. Fang, R. Wu, L. Zhao, X. Ma, X. Tian, S. Lee, C. Zhang, C. Chen, Z. Chai, C. Ge, R. Zhou, *Nat. Commun.* 2018, 9, 4861